Contents of this supplement

Text S1 to S18; Figures S1 to S9; embedded Tables S16 to S20; descriptions of machine-readable Tables S1 to S23

The analyzed observations were recorded with GPStation6 hardware. 'Monitor 02' is the current Danzhou catalogue identifier assigned after the later GISMOR upgrade; the later receiver is not part of this study. The historical data were reprocessed by the Chinese Meridian Project Data Center with the updated product algorithm. The ScienceDB record contains author-generated figure data and derived statistics and excludes official source files. The ScienceDB version 1.0.0 record was published on 31 August 2026; repository DOI: https://doi.org/10.57760/sciencedb.00zln.

Scientific evidence map. The principal physical interpretation is supported in two steps. Texts S13, S17, and S18 and Tables S16-S22 show that winter-afternoon TEC structures evolve over or pass through Hainan and remain consistent across the sampled directions. The same materials show that the summer near-midnight increase is present at repeatedly sampled locations but is much stronger in some directions and regions than in others. Text S16 and Tables S17 and S23 document the monthly transition between these two environments. The remaining supporting texts establish the sampling, processing, filter-response, and uncertainty bounds for these scientific conclusions.

Supporting Text S1. Processing definitions and complete climatology products

All supporting products use the definitions in the main manuscript. The primary VTEC result is the median across UTC-date cell medians. The primary dTEC RMS result uses a 60 min centered running-median background, a 30 min centered RMS window evaluated every 5 min, a 20° minimum elevation, a 90 s arc-gap threshold, at least 75% of nominal 30 s samples, and two-sided temporal support. Complete month-LST VTEC and dTEC RMS fields and the season-LST dTEC RMS field are provided as Tables S1-S3 in the companion data deposit.

Supporting Text S2. Coverage and solar-geomagnetic sample composition

The analysis contains 1,793 source UTC dates from 23 September 2015 through 31 December 2020. Annual contributions are 78, 364, 359, 365, 266, and 361 dates for 2015-2020. Tables S4 and S5 report year-month coverage and the represented-date distributions of F10.7, Kp, and Dst. These quantities establish the activity composition against which the seasonal organization is interpreted.

Supporting Text S3. Annual-composition sensitivity

The equal-year analysis first aggregates within year-month-LST and then gives each represented year equal weight. The common-year analysis uses 2016, 2017, 2018, and 2020, and the leave-one-year-out analysis omits each source year in turn. For VTEC, equal-year and common-year estimates retain Spearman correlations of 0.9931 and 0.9940 with the pooled climatology; for dTEC RMS, the corresponding correlations are 0.9874 and 0.9854. Leave-one-year-out correlations are

0.9976-0.9988 for VTEC and 0.9933-0.9957 for dTEC RMS. Tables S6 and S7 provide the complete cell and omission results.

Supporting Text S4. Matched VTEC-dTEC diagnostics

The matched product contains 41,111 daily cells on 1,792 UTC dates. The raw daily-cell Spearman coefficient is -0.1593, the coefficient after subtracting each month-LST median is -0.0820, and the coefficient across 276 climatology cells is -0.1644. Table S8 contains the intervals and quartile summaries. These values show that VTEC magnitude supplies little ordering of the seasonal dTEC amplitude field.

Supporting Text S5. Background- and RMS-window comparison

Five alternative combinations of 60 or 120 min backgrounds and 10, 30, or 60 min RMS windows give common-cell rank correlations of 0.8827-0.9869 and median absolute differences of 0.0018-0.0157 TECU. These alternatives remain within the running-median/RMS family. Supporting Text S12 and Figure S8 therefore add smooth-null and sinusoidal-response tests for the nonlinear reference operator.

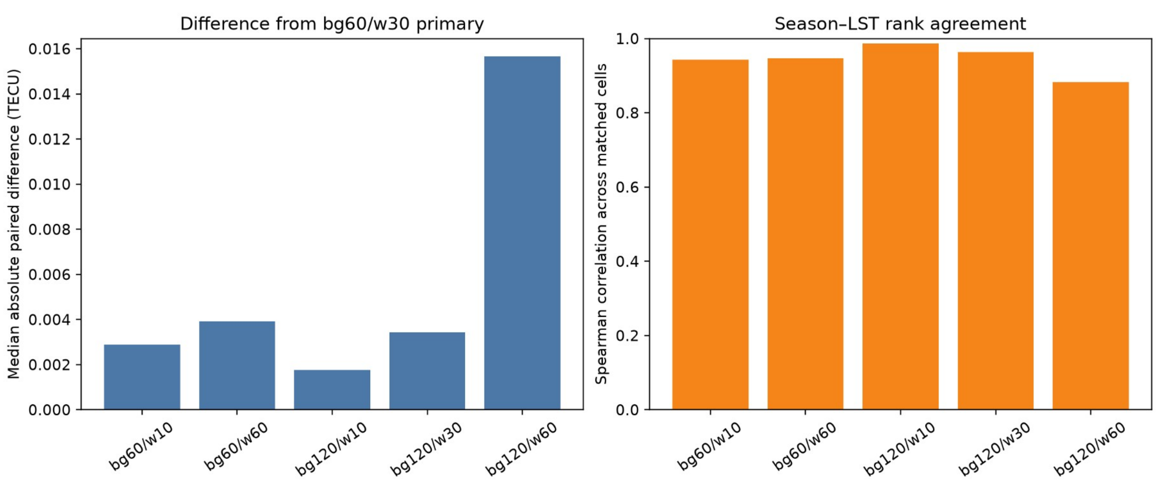

Figure S1. Complete processing-window comparison. Each panel pairs an alternative background/RMS-window configuration with the primary 60/30 min result over common season-LST cells and shows the associated differences.

Supporting Text S6. Viewing-geometry stratification

Azimuth and elevation bins show that viewing geometry contributes to local amplitude differences. The record-level IPP-speed analysis in Supporting Text S13 directly separates nearly fixed and moving paths and repeats the seasonal contrast within GPS and BeiDou samples.

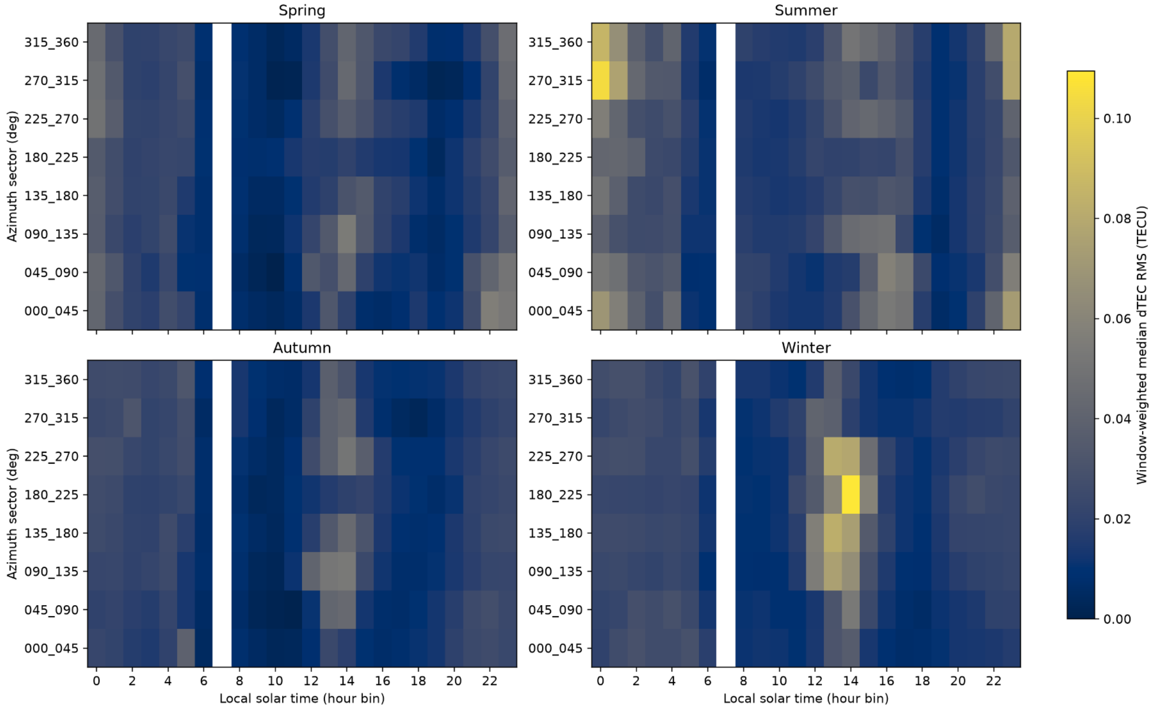

Figure S2. Azimuth-stratified dTEC RMS climatology using 45° sectors. The panels show the seasonal-local-time organization sampled in each viewing sector.

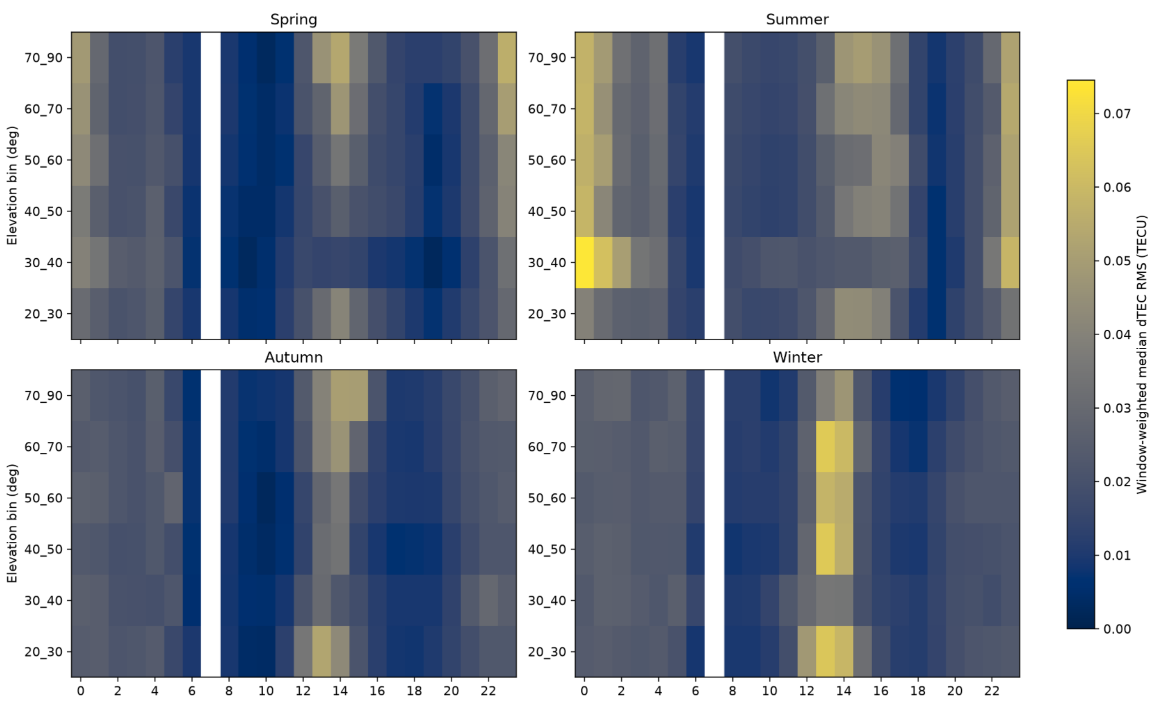

Figure S3. Elevation-stratified dTEC RMS climatology for 20°-30°, 30°-40°, 40°-50°, 50°-60°, 60°-70°, and 70°-90° bins.

Supporting Text S7. Record-level elevation and arc-gap sensitivity

Minimum-elevation and arc-gap alternatives were recomputed before arc construction, background estimation, and RMS calculation. Elevation thresholds of 25°, 30°, and 35° relative to 20° yield across-cell median absolute differences of 0.000209-0.000447 TECU and rank correlations of 0.9948-0.9982. Arc gaps of 60, 120, and 300 s relative to 90 s yield differences of 0.000028-0.000106 TECU and correlations of 0.9996-0.9999. The largest local elevation-threshold difference occurs in spring at LST 14, but the source-UTC winter-afternoon and spring-summer late-evening/midnight organization remains recognizable. Table S10 contains the complete grid.

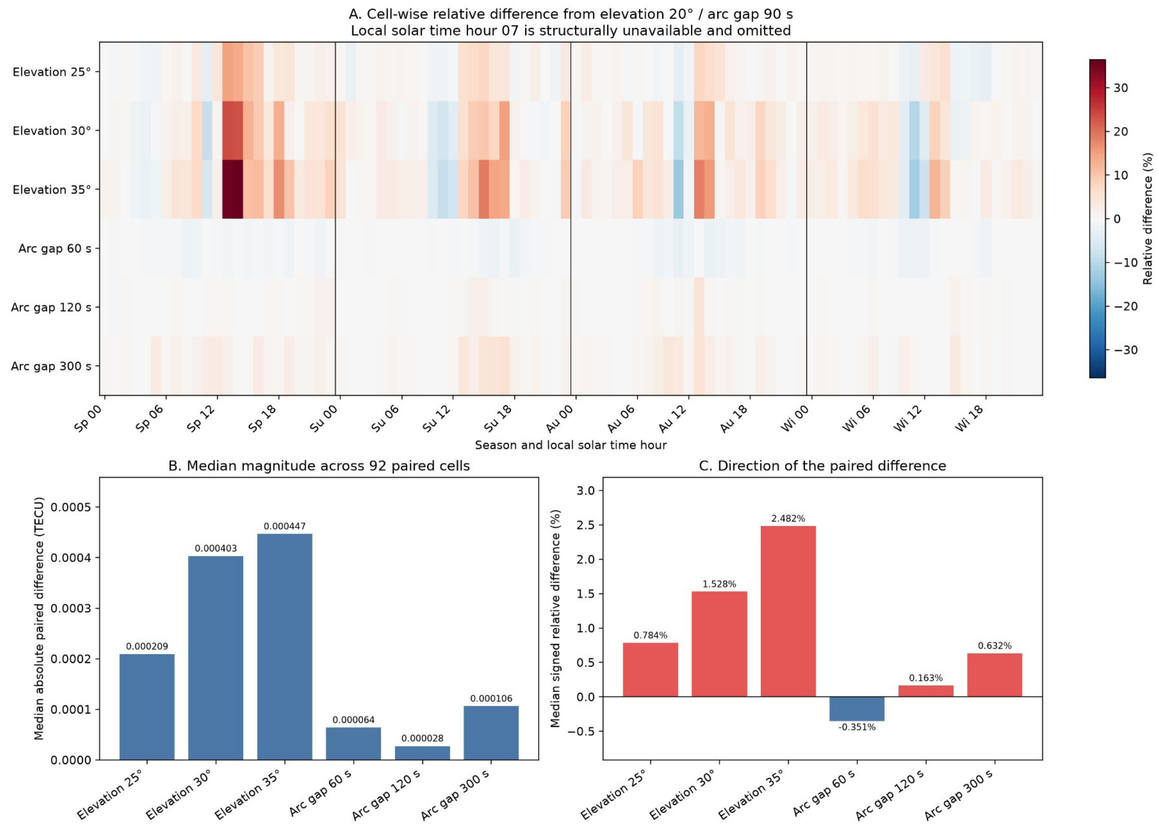

Figure S4. Complete local sensitivity maps for record-level minimum-elevation and arc-gap alternatives relative to the primary 20°/90 s configuration.

Supporting Text S8. Daily-product boundary support

The centered analysis splits arcs at the UTC-date boundary so that the reproducible daily-product discontinuity does not enter dTEC. Relative to the boundary-unsafe implementation, boundary-safe processing removes 995,382 of 6,546,286 candidate primary windows and retains 5,550,904. Annual removal fractions range from 14.70% to 15.90%. Across the expected 384 month/season-LST cells, 16 are unavailable, all at LST 07, as dictated by the station longitude, source-product boundary, and two-sided support requirement. Table S11 provides the full audit.

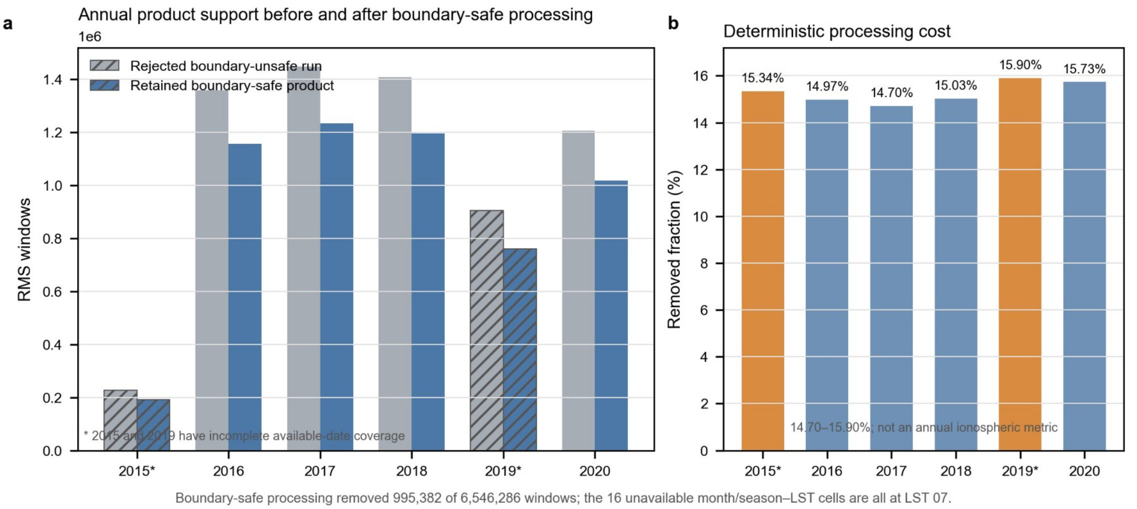

Figure S5. Annual support before and after UTC-boundary-safe processing, including candidate, removed, and retained-window counts and annual removal fractions.

Supporting Text S9. Date-basis, activity, and aggregation controls

Source UTC dates compare LST 12-16 with 21-00. Local-calendar dates compare LST 12-16 with 21-23 on the same local date. Observation nights assign LST 00-02 to the preceding evening and support broad and equal-width comparisons. Hourly tests compare LST 21, 22, 23, 00, and 01 with the LST 12-16 anchor.

The local-calendar summer interval includes zero: the LST 21-23 minus 12-16 median is -0.002025 TECU with a 95% interval of -0.004524 to 0.000311 TECU. Observation-night analysis gives positive summer differences at LST 23, 00, and 01. The equal-width LST 23-00 minus 13-14 contrast is 0.015362 TECU (0.010813-0.020446; 458 dates) and 0.016498 TECU in the activity-restricted subset.

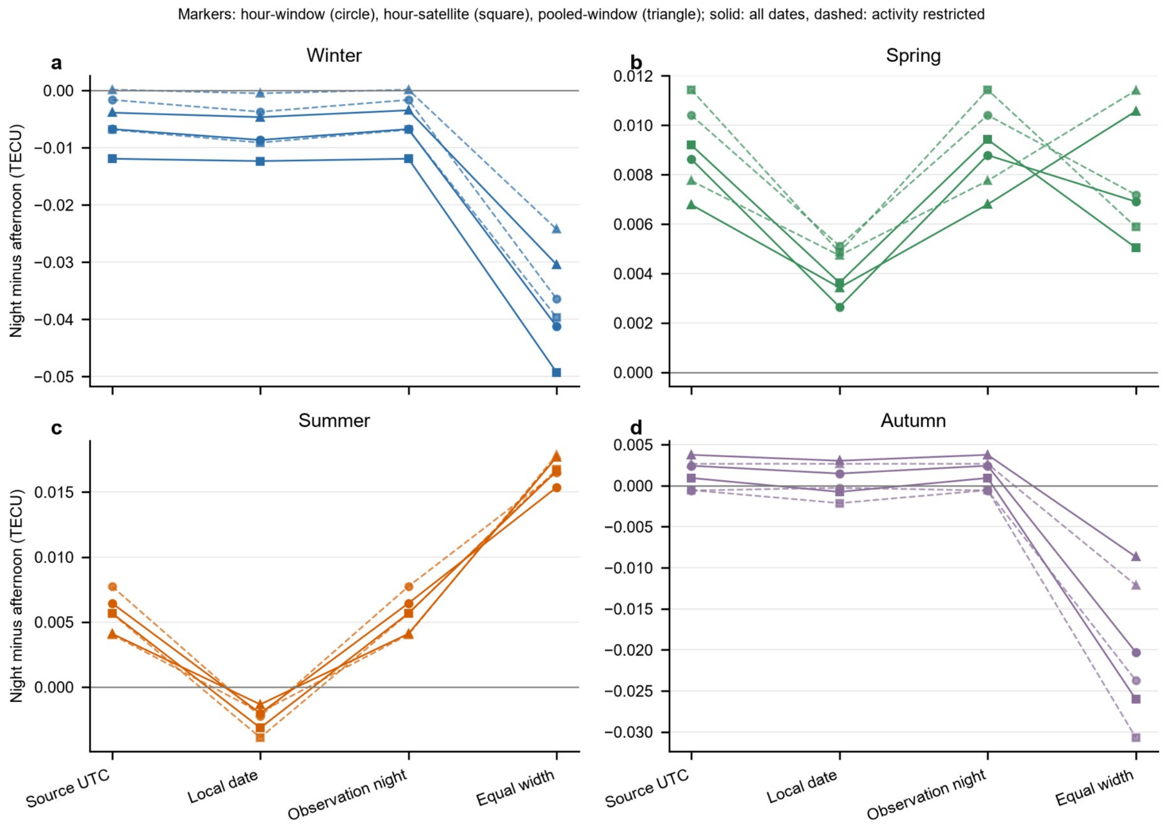

Figure S6. Aggregation and activity sensitivity of the seasonal contrasts. Results are shown for hourly-window medians, equal weighting of satellite-specific hourly medians, and pooled sector windows, with unrestricted and fixed Kp-Dst-F10.7 subsets. The winter and summer directions are preserved.

Supporting Text S10. Illustrative cases and trace eligibility

The six cases provide trace-level illustrations under fixed coverage and amplitude conditions. Winter uses LST 12-16 as the target and 21-00 as the control; summer uses LST 23-00 and the equal-width LST 13-14 control. Both sectors require at least 80% coverage, three continuously supported satellites, a largest-satellite share below 20%, and a positive target-minus-control contrast. Candidates are restricted to the 75th-90th percentile of target amplitude and ranked by coverage and satellite support.

The selected winter dates are 2 December 2017, 23 February 2019, and 18 December 2018; summer dates are 11 August 2017, 17 June 2016, and 22 June 2020. Figure S7 displays every eligible trace. Highlighted curves are chosen by coverage and elevation proximity to 55°. Because the selection favors clear target-sector examples, these dates are illustrative rather than an independent validation set.

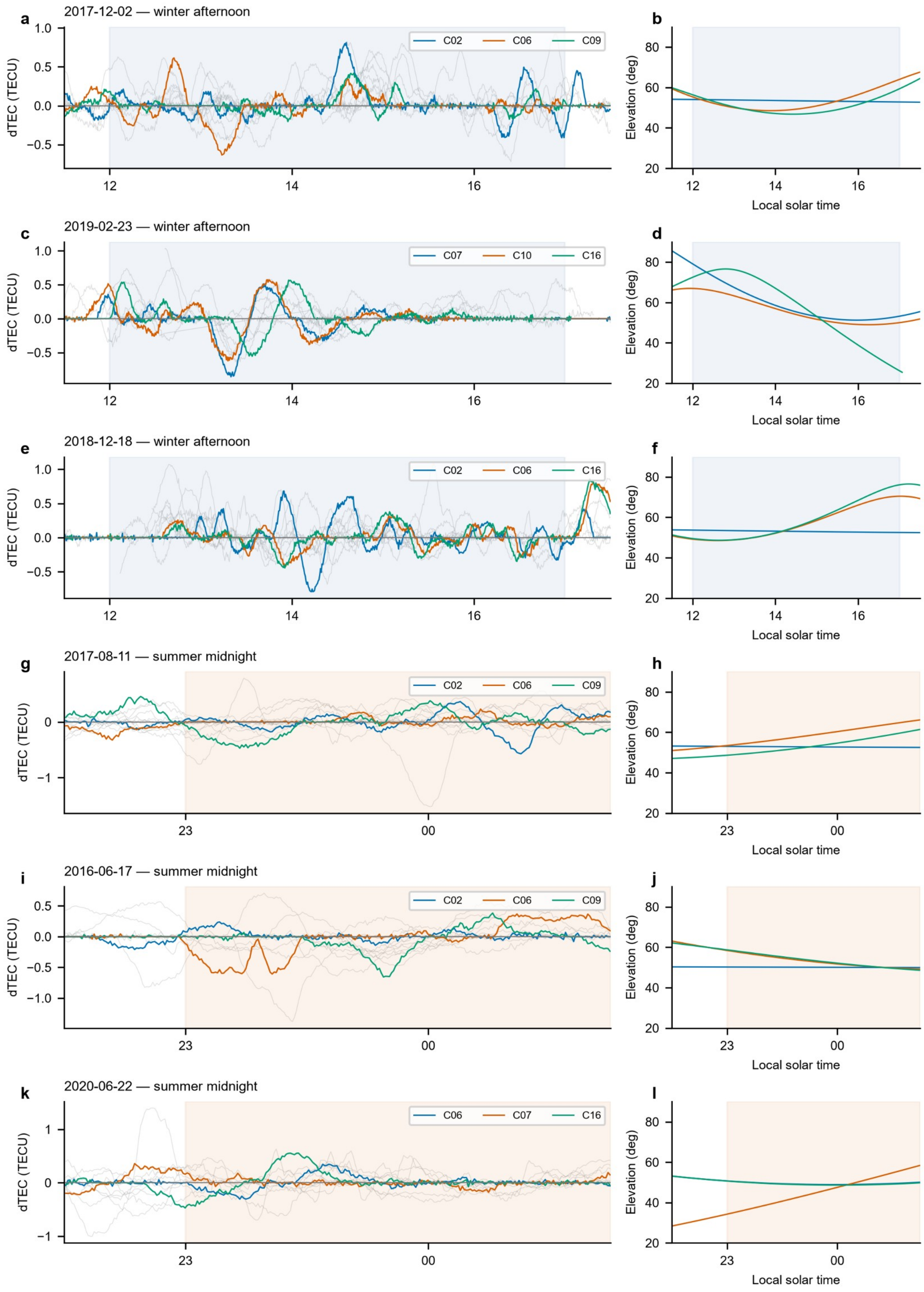

95

Figure S7. Complete illustrative winter and summer case set. Each row shows eligible satellite-specific dTEC traces and elevation for one selected date. Shading identifies the target sector.

Supporting Text S11. Reproducibility checks

The analysis processes 5,550,904 boundary-safe dTEC RMS windows from a versioned YAML configuration. Five unit tests cover date assignment, seasonal aggregation, and case-selection calculations. All reported date definitions are retained in the outputs, including the local-calendar summer interval spanning zero.

A separate implementation recomputed the 16 primary seasonal/date-layer groups. The maximum absolute difference from the main output was 9.84×10^{-17} TECU. The software archive contains configuration, tests, expected results, and the independent check; the data record contains machine-readable outputs and SHA-256 checksums.

Machine-readable tables in the ScienceDB record

Table S1. Complete month-LST VTEC climatology.

Table S2. Complete month-LST dTEC RMS climatology.

Table S3. Complete season-LST dTEC RMS climatology.

Table S4. Year-month source-date coverage.

Table S5. Activity-index composition on represented dates.

Table S6. Pooled, equal-year, and common-year month-LST cells.

Table S7. Leave-one-year-out comparisons.

Table S8. Matched daily and climatology-cell VTEC-dTEC diagnostics.

Table S9. Complete background/RMS-window paired metrics and cells.

Table S10. Complete record-level elevation and arc-gap sensitivity grid.

Table S11. UTC-boundary support and structurally unavailable-cell audit.

Table S12. Sector-summary table containing all date assignments, activity subsets, and aggregation modes.

Table S13. Hour-resolved observation-night date-level and seasonal-summary files for LST 21, 22, 23, 00, and 01.

Table S14. Illustrative case-selection ledger, including eligibility and ranking fields.

Table S15. Case trace summary and file map for the satellite traces used in Figures 6 and S7.

The formal repository citation is provided in the main manuscript. The ScienceDB version 1.0.0 record includes machine-readable support for Tables S1-S15 and Figures S1-S9, file-level SHA-256 values, and a source map.

Supporting Text S12. Smooth-null leakage and sinusoidal response

Twenty-four dates were selected by coverage alone, six per season. The validation includes 192 satellite arcs of at least 4 h, with nearly fixed and moving IPPs represented where available. Cubic polynomials and cubic splines with 180 min knots were passed through the 60 min running-median and 30 min RMS chain. Median RMS is commonly zero along monotonic portions of a smooth arc, while the arc-level 95th-percentile leakage near curvature extrema is approximately 0.01-0.04 TECU. In the six summer dates, the moving-IPP spline smooth-null sector difference has a median of 0 and a 10th-90th percentile range of -0.0066 to 0.0115 TECU. The corresponding near-fixed spline baseline also has a median of 0, with a 10th-90th percentile range of -0.00546 to 0.00369 TECU; the cubic-polynomial near-fixed baseline is negative, with a median of -0.00461 TECU. Neither near-fixed smooth model produces a date-level absolute difference as large as the key summer equal-width contrast in these six dates. Thus the observed positive near-fixed summer contrast is not the preferred sign of smooth-background leakage, although this small validation sample does not define a universal error distribution.

Sinusoids were injected into 48 spline backgrounds at periods of 20-120 min, amplitudes of 0.02-0.10 TECU, and four phases, giving 3,456 runs. The incremental amplitude response depends on background slope and injected amplitude. Recovery generally decreases toward 90-120 min because the 60 min median follows more of the slow variation.

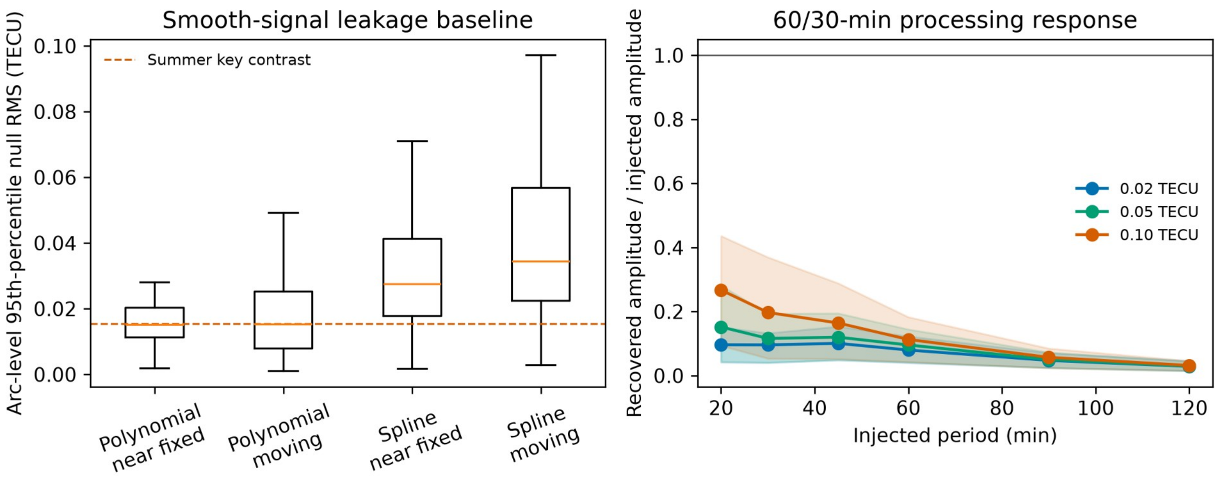

Figure S8. Smooth-signal leakage and response of the 60/30 min operator. The left panel shows arc-level 95th-percentile RMS generated from smooth inputs; the horizontal line is the observed summer equal-width contrast. The right panel shows recovered sinusoidal amplitude relative to injected amplitude.

Supporting Text S13. Physical basis and primary IPP comparison

The primary IPP comparison asks whether each seasonal enhancement changes with time at one ionospheric location or also varies across the surrounding region. Nearly fixed paths move at no more than 0.2 km/min and moving paths at no less than 0.5 km/min on a 450 km thin shell; intermediate speeds are excluded. The same-date contrast compares LST 23-00 with LST 13-14. Winter is afternoon-dominant in both motion classes, including after elevation and azimuth are jointly matched. This shared winter response requires temporal evolution or passage through the sampled region. Summer remains night-dominant at nearly fixed IPPs, establishing a temporal near-midnight increase, while its amplitude changes more strongly with sampled direction and region. Elevation matching retains 442 summer and 385 winter dates; joint elevation-azimuth matching retains 114 summer and 174 winter dates. Table S16 reports the complete estimates and date-bootstrap intervals.

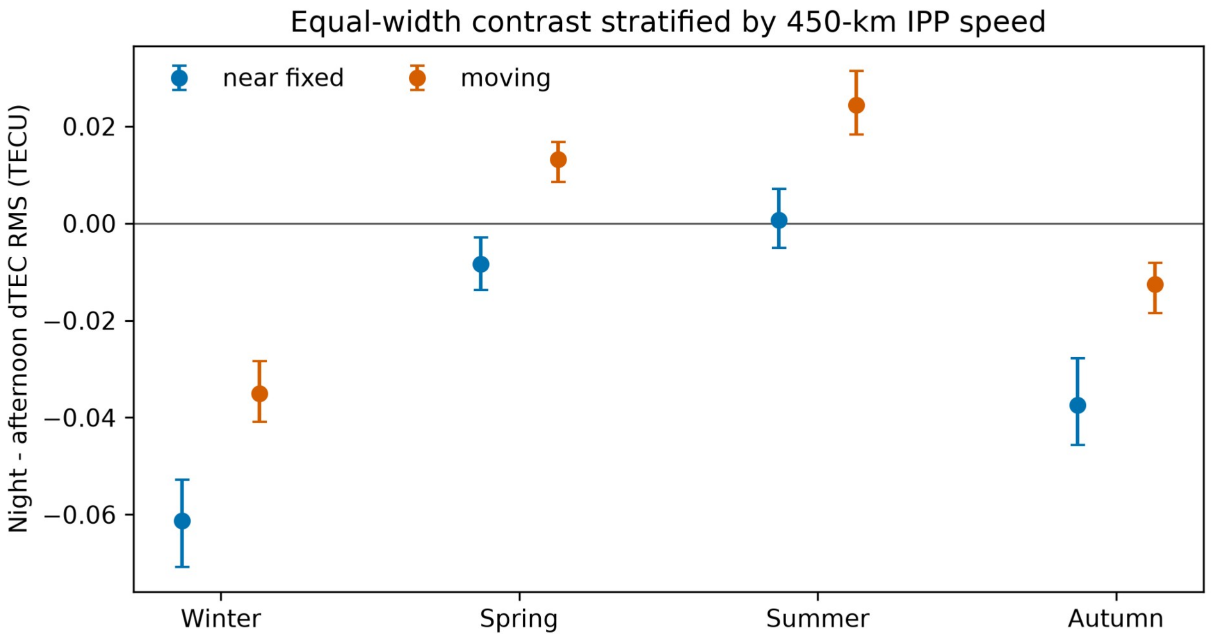

Figure S9. Unbalanced diagnostic contrasts for nearly fixed and moving 450-km IPPs. Error bars are 95% date-bootstrap intervals. Positive values favor LST 23-00 and negative values favor LST 13-14. The matched primary comparisons are reported in Table S16 and in the main manuscript.

Supporting Text S14. Satellite support, date dependence, and strict-match support

The 41,119 daily month-LST cells contain a median of 13 satellites and 141 valid windows. At least 3, 5, and 8 satellites retain 99.87%, 99.26%, and 96.78% of cells, and the eight-satellite field has Spearman rho = 0.9987 relative to the one-satellite baseline. Lag-one correlations of the equal-width date-level contrast are 0.34 in winter, 0.26 in spring, 0.02 in summer, and 0.06 in autumn. Moving blocks of 3, 5, and 7 days preserve all seasonal signs. The strict elevation-azimuth leave-one-satellite subsets are less uniform: some contain only 7-24 paired dates. Those subsets diagnose direction and satellite dependence but are not used as replacements for the full climatology or the full strict comparison.

Supporting Text S15. Historical receiver and current product identifier

The analyzed 2015-2020 observations were recorded with a GPStation6 receiver. The later GISMOR receiver is not used. 'Monitor 02' is the current Danzhou catalogue identifier assigned after the phase-II upgrade. The Chinese Meridian Project Data Center reprocessed the historical GPStation6 observations with the same updated algorithm used for the phase-II product; Yusen Tian was the responsible data producer. Only GPS and BeiDou records enter the analysis.

Additional machine-readable tables in this supplement

Tables S1-S15 are described above and are contained in the ScienceDB version 1.0.0 record. Tables S16-S23 accompany the current IPP analysis: primary geometry-matched contrasts (S16), transition-month estimates (S17), orbit-group contrasts (S18), individual-satellite contrasts (S19), leave-one-satellite stability ranges (S20), complete leave-one-satellite results (S21), satellite composition (S22), and month-specific geometry support (S23). Tables S16-S20 are reproduced below; Tables S21-S23 are supplied as machine-readable CSV files.

Supporting Text S16. Monthly transition between the winter and summer environments

The monthly IPP comparison follows the replacement of the winter-afternoon disturbance environment by the warm-season near-midnight environment. Under elevation matching, March retains an afternoon-dominant nearly fixed signal, April lies near the crossover, and both classes are night-dominant by May. September retains a weak night-dominant component, October is near the crossover, and November is afternoon-dominant in both classes. The observations therefore record an ordered spring transition and its autumn reversal, rather than two uniform intermediate seasons. Table S17 reports estimates, intervals, and paired-date counts.

Supporting Text S17. Winter consistency and summer directional variation

The orbit and single-satellite results clarify the horizontal character of the two seasonal enhancements. Near-fixed windows are almost entirely contributed by BeiDou GEO satellites, whereas moving windows are dominated by IGSO satellites with limited MEO support. GEO and IGSO groups both show winter-afternoon and summer near-midnight enhancement in aggregate. Adequately sampled winter GEO satellites share the same afternoon-dominant sign, supporting a disturbance pattern that evolves over Hainan across the sampled directions. Summer individual-satellite estimates are much more heterogeneous: some directions show a clear near-midnight increase, whereas others lie near zero or have the opposite sign. This directional variation supports a summer enhancement that is concentrated in particular regions or directions rather than spread uniformly. MEO same-date support is insufficient for a separate orbit-specific conclusion. Tables S18, S19, and S22 provide the complete orbit, PRN, and composition results.

Supporting Text S18. Direction-matched evidence for the winter and summer interpretations

Removing any one of the 16 observed BeiDou satellites preserves the elevation-matched winter and summer signs, so neither seasonal pattern is carried by one PRN. Joint elevation-azimuth matching then separates the physical interpretations. Winter remains afternoon-dominant in both motion classes and the two estimates agree within uncertainty, supporting structures that evolve with time over or pass through Hainan. In summer, the moving estimate spans zero while the nearly fixed estimate remains positive, and the moving-minus-nearly-fixed estimate becomes negative. The broad-sample moving advantage therefore reflects the directions and regions sampled by those paths rather than an effect of motion speed. No satellite deletion restores a positive moving-path advantage. The full strict comparison retains 114 summer and 174 winter dates; several deletion subsets have limited common support and are treated only as supporting diagnostics. Tables S20 and S21 provide the stability ranges and complete results.

Table S16. Primary geometry-matched same-date contrasts. Values are medians in TECU with 95% date-bootstrap intervals.

Season	Geometry	n	Moving	Nearly fixed	Moving - fixed
Winter	Elevation	385	-0.02583 [-0.03564, -0.01657]	-0.05219 [-0.06852, -0.03991]	0.01614 [0.01056, 0.02378]
Summer	Elevation	442	0.02128 [0.01711, 0.02600]	0.00823 [0.00464, 0.01222]	0.01738 [0.01214, 0.02424]
Winter	Elevation + azimuth	174	-0.06030 [-0.09021, -0.02526]	-0.05353 [-0.07321, -0.04060]	-0.00458 [-0.01745, 0.00489]
Summer	Elevation + azimuth	114	0.00169 [-0.01843, 0.01732]	0.01691 [0.00505, 0.03271]	-0.02666 [-0.05152, -0.00300]

Table S17. Month-by-month direct and elevation-matched contrasts. Values are medians in TECU with 95% date-bootstrap intervals.

Month	Analysis	n	Moving	Nearly fixed	Moving - fixed
3	Direct	141	0.00149 [-0.00882, 0.00761]	-0.01962 [-0.03274, -0.00831]	0.02539 [0.01591, 0.03845]
3	Elevation matched	141	0.00333 [-0.00112, 0.01246]	-0.01098 [-0.01769, -0.00161]	0.01492 [0.00668, 0.02726]
4	Direct	147	0.00876 [0.00154, 0.01410]	-0.01515 [-0.02222, -0.00666]	0.01488 [0.00545, 0.02556]
4	Elevation matched	146	0.00762 [0.00100, 0.01228]	0.00330 [-0.00337, 0.00783]	0.00661 [-0.00215, 0.01634]
5	Direct	154	0.02051 [0.01097, 0.03997]	0.01398 [-0.00036, 0.02287]	0.01248 [0.00457, 0.02042]
5	Elevation matched	141	0.02240 [0.01433, 0.03474]	0.02165 [0.01420, 0.03581]	0.00456 [-0.00502, 0.01214]
9	Direct	131	0.00593 [0.00087, 0.01538]	-0.00707 [-0.01803, 0.00126]	0.01137 [0.00729, 0.01986]
9	Elevation matched	124	0.00904 [0.00478, 0.01678]	-0.00191 [-0.00963, 0.00600]	0.01088 [0.00254, 0.01667]
10	Direct	139	-0.02411 [-0.03081, -0.01527]	-0.03692 [-0.04841, -0.02220]	0.01397 [0.00519, 0.02617]
10	Elevation matched	134	-0.00236 [-0.01891, 0.00476]	0.00117 [-0.01948, 0.00436]	0.01236 [0.00410, 0.02180]
11	Direct	145	-0.02419 [-0.03741, -0.01924]	-0.08208 [-0.09865, -0.06562]	0.03968 [0.02886, 0.05604]
11	Elevation matched	144	-0.01201 [-0.02346, -0.00180]	-0.07005 [-0.08388, -0.04661]	0.03145 [0.02103, 0.05429]

Table S18. Orbit-group night-minus-afternoon contrasts. MEO estimates are descriptive because same-date support is sparse.

Orbit	Season	n	Contrast, TECU [95% CI]	Night > afternoon
GEO	Summer	450	0.00508 [0.00035, 0.00985]	0.551
GEO	Winter	417	-0.04666 [-0.05771, -0.03313]	0.240
IGSO	Summer	449	0.02371	0.728

Orbit	Season	n	Contrast, TECU [95% CI]	Night > afternoon
			[0.01910, 0.03007]	
IGSO	Winter	446	-0.02810 [-0.03615, -0.02154]	0.291
MEO	Summer	18	-0.03399 [-0.10967, 0.06909]	0.444
MEO	Winter	9	0.00000 [-0.15301, 0.01016]	0.444

Table S19. Individual-PRN contrasts with at least 30 paired dates.

PRN	Orbit	Season	n	Contrast, TECU [95% CI]
C01	GEO	Summer	443	0.00471 [-0.00014, 0.00856]
C01	GEO	Winter	375	-0.03901 [-0.05416, -0.02959]
C02	GEO	Summer	336	0.00970 [0.00504, 0.01721]
C02	GEO	Winter	309	-0.05088 [-0.06900, -0.03685]
C03	GEO	Summer	313	0.01274 [0.00901, 0.02038]
C03	GEO	Winter	299	-0.05815 [-0.07364, -0.04365]
C04	GEO	Summer	302	-0.00402 [-0.00828, -0.00012]
C04	GEO	Winter	323	-0.03308 [-0.04203, -0.01851]
C05	GEO	Summer	116	0.00387 [-0.00076, 0.01070]
C05	GEO	Winter	76	-0.04711 [-0.08169, -0.01957]
C06	IGSO	Summer	241	0.03918 [0.03191, 0.04683]
C06	IGSO	Winter	94	0.00435 [-0.00011, 0.01306]
C07	IGSO	Summer	290	0.02083 [0.01451, 0.02821]
C07	IGSO	Winter	397	-0.02332 [-0.03535, -0.01418]
C08	IGSO	Summer	166	-0.01887 [-0.03536, -0.01118]
C08	IGSO	Winter	67	0.00989 [0.00542, 0.01233]
C09	IGSO	Summer	196	0.04475 [0.03479, 0.05438]
C09	IGSO	Winter	47	-0.02914 [-0.08570, 0.00001]
C10	IGSO	Summer	208	0.02183 [0.01431, 0.02841]
C10	IGSO	Winter	372	-0.02792 [-0.04121, -0.01358]
C13	IGSO	Summer	169	-0.00613 [-0.01201, 0.00013]

PRN	Orbit	Season	n	Contrast, TECU [95% CI]
C13	IGSO	Winter	80	-0.02385 [-0.04248, -0.01214]
C15	IGSO	Summer	68	-0.00152 [-0.01549, 0.00555]
C16	IGSO	Summer	142	0.04652 [0.03295, 0.05650]
C16	IGSO	Winter	55	0.00669 [-0.02105, 0.01849]

Table S20. Leave-one-PRN stability ranges across the 16 satellite omissions.

Geometry	Season	n min	n max	Moving median range, TECU
Elevation	Summer	403	442	0.01899 to 0.02516
Elevation	Winter	314	385	-0.03443 to -0.02182
Elevation + azimuth	Summer	7	114	-0.09502 to 0.01389
Elevation + azimuth	Winter	7	174	-0.06851 to -0.03587